Experimental and first-principles investigation of the electronic structure anisotropy of Cr_2AlC

M. Bugnet,[1,2,*] M. Jaouen,[1,†] V. Mauchamp,[1] T. Cabioc'h,[1] and G. Hug[3]

[1]*Institut PPRIME, UPR 3346 CNRS–Université de Poitiers–ISAE-ENSMA, Département de Physique et Mécanique des Matériaux, SP2MI Téléport 2, Boulevard Marie et Pierre Curie, Boîte Postale 30179, 86962 Futuroscope-Chasseneuil Cedex, France*

[2]*Department of Materials Science and Engineering, McMaster University, 1280 Main Street West, Hamilton, Ontario, Canada L8S 4L7*

[3]*Laboratoire d'Etudes des Microstructures, CNRS-ONERA, Boîte Postale 72, 92322 Châtillon Cedex, France*

(Received 21 May 2014; revised manuscript received 11 October 2014; published 11 November 2014)

The anisotropy of the electronic structure of the *MAX* phase Cr_2AlC has been investigated by electron-energy-loss spectroscopy (EELS) at the C *K* edge, and x-ray-absorption spectroscopy (XAS) at the Al *K*, Cr $L_{2,3}$, and Cr *K* edges. The experimental spectra were interpreted using either a multiple-scattering approach or a full-potential band-structure method. The anisotropy is found to be small around C atoms because of the rather isotropic nature of the octahedral site, and of the averaging of the empty C *p* states probed by EELS at the C *K* edge. In turn, a pronounced anisotropy of the charge distribution around Al atoms is evidenced from polarized XAS measurements performed on textured Cr_2AlC sputtered thin films. From the analysis of the XAS data using the multiple-scattering FEFF code, it is demonstrated that the probed thin film is constituted of 70% (0001) and 30% $(10\bar{1}3)$ grains oriented parallel to the film surface. A decomposition of the calculated spectrum in coordination shells allows for the ability to connect XAS fine structures to the Cr_2AlC structure. Combining high-resolution data with up-to-date multiple-scattering calculations, it is shown that the crystalline orientations of the grains present in a probe of $100 \times 100\ \mu m^2$ can be determined from the Cr *K* edge. Interestingly, it is also revealed that a static disorder is involved in the studied thin films. These findings highlight that, given the overall agreement between experimental and calculated spectra, the Cr_2AlC electronic structure is accurately predicted using density functional theory.

DOI: 10.1103/PhysRevB.90.195116 PACS number(s): 78.70.Dm, 79.20.Uv, 61.05.cj

I. INTRODUCTION

Discovered 50 years ago in Vienna [1], Cr_2AlC has received intense attention both experimentally and theoretically [2–6], especially because of its very good resistance to oxidation and corrosion, and its high elastic stiffness [7–15]. This compound, whose unit cell is shown in Fig. 1, is the prototype of a wide family of ternary carbides and nitrides now known as *MAX* phases. These materials represent a class of solids that can be described as thermodynamically stable nanolaminates [16]. They have been intensively investigated due to their unique combination of properties of ceramics and metals [17–19]. Their general chemical formula is $M_{n+1}AX_n$, where M is an early transition metal, A is an A-group element, X is either C or N, and $n = 1$, 2, or 3. Depending on the stoichiometry, three different crystal structures are obtained and classified as 211 ($n = 1$), 312 ($n = 2$), and 413 ($n = 3$). All crystallize in a hexagonal structure (space group $P6_3/mmc$) presenting quite large c/a ratios. For $n = 1$, the c/a ratio ranges from 3.5 to 4.6 (it is 4.48 for Cr_2AlC), while for $n = 2$ and 3 the c/a ratios range from ≈5.8 to 6 and 7.7 to 7.8, respectively.

This highly anisotropic crystal structure is the reason for some of their unusual transport/dielectric properties. For instance, the negligible Seebeck coefficient of polycrystalline Ti_3SiC_2 [20] was shown to arise from the combination of a negative value along the c axis and a positive one in the basal planes of the hexagonal structure [21]. Moreover, it has been shown that the electrical conductivity anisotropy evidenced in Ti_2GeC [22], Cr_2GeC [23], and Ti_2AlC [24] varies as a function of the chemical composition. The investigation of the anisotropy in *MAX* phase dielectric properties has also been studied combining valence electron-energy-loss spectroscopy (VEELS) experiments in a transmission electron microscope (TEM) and *ab initio* calculations based on the density functional theory (DFT) [25–28]. However, the signal measured in such approaches is not atomic-species-selective: accessing the atomic selectivity requires the use of elemental probes, and it can be achieved from core-level spectroscopies using either electrons (EELS) or x rays. In the latter case, the experiments can be performed either in emission [x-ray emission spectroscopy (XES)] or in absorption [x-ray absorption spectroscopy (XAS)]. XES and XAS, combined with first-principles calculations, were used to study the electronic structure of Ti_2AlC [29], Ti_2AlN [30], Ti_4SiC_3 [31], Ti_3AlC_2, Ti_3SiC_2, and Ti_3GeC_2 [32]. However, studies specifically dedicated to electronic structure anisotropy and polarization-dependent core-level spectroscopies have been limited to V_2GeC [33], Ti_3SiC_2 [34], and Ti_3AlC_2 [35]. The spectroscopic data (EELS, XES, or XAS) are generally compared to the local density of states (LDOS) obtained from band-structure calculations, which do not include the core-hole effect [36] inherently involved in such experiments. In this paper, the anisotropy of Cr_2AlC electronic structure is investigated using *ab initio* calculations in order to interpret the fine structures (FSs) observed on polarization-dependent core-level spectra.

II. EXPERIMENTAL DETAILS

Since *MAX* phase single crystals have only been synthesized as thin films or as small free-standing crystals [37], probing their anisotropy experimentally remains a

---

[*] bugnetm@mcmaster.ca

[†] Deceased.

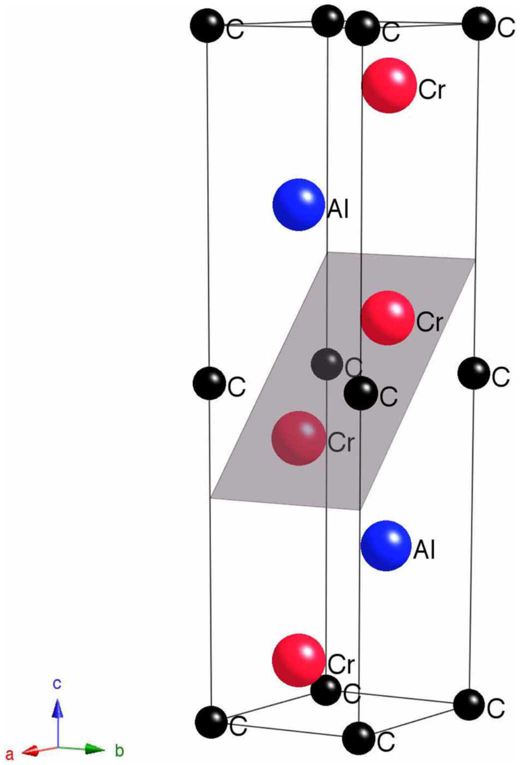

FIG. 1. (Color online) Cr_2AlC unit cell. Light gray: $(10\bar{1}3)$ planes.

challenge [38,39]. Nevertheless this achievement is possible within the TEM with the drawback that the magnitude of the measured EELS signal strongly decreases when the energy loss increases. Therefore, only the C K edge was probed using this technique. The Al K, Cr $L_{2,3}$, and Cr K edges were acquired on thin films using polarized x-ray from synchrotron radiation (SR) facilities.

A. Samples description

1. *Bulk Cr_2AlC sample*

The C K edge was obtained on a bulk polycrystalline Cr_2AlC sample synthesized by standard hot isostatic pressing method, starting from subsequently dry mixed and cold pressed Cr, Al, and C powders; details about the synthesis methods are given elsewhere [40]. The typical grain size is in the order of 100 μm. The TEM specimen were cut using a diamond saw and then thinned down to 10 μm by tripod polishing. Electron transparency was reached by argon ion milling with a Gatan precision ion polishing system (PIPS) operated at 2.5 kV and ion beams at ±8°. A final step was applied at a grazing incidence of ±4°. The lattice parameters obtained from powder neutron diffraction data [40] were $a = 2.86$ Å and $c = 12.81$ Å. These values will be used for all simulations presented in Sec. IV, while for the free internal parameter z_{Cr}, the value obtained from the DFT optimizations of Keast *et al.* is chosen ($z_{\mathrm{Cr}} = 0.085$) [41].

2. *Cr_2AlC thin films*

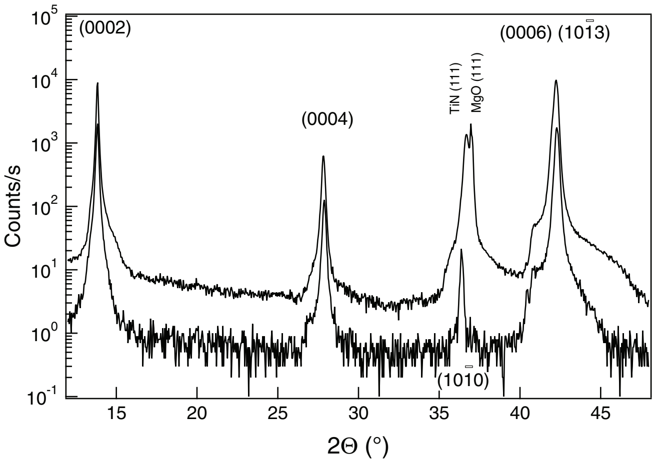

FIG. 2. XRD spectra of Cr_2AlC thin films deposited onto $Al_2O_3(0001)$ (S1, bottom) and MgO(111)/TiN(111) (S2, top).

Two Cr_2AlC thin films have been deposited by magnetron sputtering, a now well-established method for *MAX* phase thin-film deposition [38]. One sample was deposited onto (0001)-oriented sapphire (S1) and a second deposited onto MgO(111) with a TiN(111) seed layer (S2) to favor epitaxy. Both substrates, 1 × 1 cm^2 in size, were ultrasonically degreased in acetone then in ethanol for 5 min before deposition from elemental Cr (99.95% purity), Al (99.999%), and graphite (99.999%) targets mounted in an experimental setup described elsewhere [42]. The base pressure was less than 5×10^{-6} Pa and the sputtering gas was Ar (99.999% purity) at a pressure of ~0.3 Pa. The Cr ($P_{\mathrm{Cr}} = 60$ W) and C ($P_{\mathrm{C}} = 200$ W) targets were run in dc power-control mode, while the Al [$P_{\mathrm{Al}} = 90$ W (S1) or 100 W (S2)] target was rf-sputtered. The deposition temperature at the substrate surface was ~700 °C and the deposition time was 30 min leading to film thicknesses of ~190 nm. The θ-2θ x-ray diffraction (XRD) patterns recorded in Bragg-Brentano geometry for S1 and S2 is shown in Fig. 2 (log scale). These θ-2θ diffractograms were carried out in a Bruker D8 diffractometer using Cu $K\alpha$ radiation with an incidence angle slightly offset ($\omega = +0.4°$) in order to reduce the substrates' contribution. The four diffraction peaks observed in Fig. 2 for sample S1 (bottom) correspond to the 0002, 0004, $10\bar{1}0$, and 0006 or $10\bar{1}3$ peaks of Cr_2AlC. For sample S2 (top), in addition to the MgO(111) and TiN(111) seed layer contributions, only 0002, 0004, and 0006 or $10\bar{1}3$ peaks are visible. These two last peaks cannot be distinguished due to a too narrow angular separation ($\Delta 2\theta \sim 0.12°$ from JCPD card No. 29-0017). The sample S2 pole figure {0002} (not shown) shows an intense diffraction peak for χ and $\varphi = 0°$ with six weak (intensity 70 times lower) diffraction spots for $\varphi = 60°$ indicating that there exists a few grains with an orientation $(10\bar{1}3)$ parallel to the surface. From this result, the thin-film sample S2 is essentially epitaxially grown with the usual [38] orientation relationship: $\mathrm{MgO}(111)\langle 1\bar{1}0\rangle \parallel Cr_2AlC(0001)\langle 11\bar{2}0\rangle$. In addition, for sample S1, a small contribution of diffracted intensity from $(10\bar{1}0)$ planes oriented parallel to the surface is detected in the θ-2θ XRD pattern.

B. Electron-energy-loss spectroscopy

ELNES (energy-loss near-edge structure) spectra at the C K edge were recorded in imaging mode using parallel illumination in a JEOL 2200FS TEM operated at 200 kV and equipped with an in-column Omega energy filter. The energy resolution as given by the full width half maximum of the elastic peak recorded without a sample was 1.2 eV. The raw spectra were corrected from noise and gain by the automatic routine of the Gatan Digital Micrograph software. The C *K* spectra were deconvolved from multiple scattering with the standard Fourier-ratio technique [43] by using a low energy-loss spectrum recorded in the same experimental conditions. The grain size is large compared to the electron probe size, and thus single grains with well-defined orientation, determined from electron diffraction patterns, were selected. To investigate the anisotropy, two experimental spectra were acquired with a collection semiangle of 7 mrad either in $[11\bar{2}0]$ zone axis (the electron beam is parallel to the Cr_2AlC basal $\{a,b\}$ plane) or in [0001] zone axis (the electron beam is parallel to the *c* axis).

C. X-ray-absorption spectroscopy

Polarized XAS experiments at the Al *K* edge were performed in the XANES (x-ray-absorption near-edge structure) energy range at the SOLEIL SR facility, on the soft-x-ray beamline LUCIA [44,45]. To avoid any contribution from the substrate, the Cr_2AlC thin-film sample S2 presented in Sec. II A 2 was selected, and the anisotropy of the charge distribution along the *c* axis and within the $\{a,\ b\}$ planes was probed using two geometries, taking advantage that the x-ray beam is linearly polarized in the horizontal plane. In the first geometry, the sample's surface was in the horizontal plane such that the incident beam hits the sample at grazing incidence (3–4°). For this in-plane geometry, the electric field $\vec{E}$ of the incoming x rays is in the sample's surface, hence probing essentially the $\{a,b\}$ basal planes, due to the texture of the film (Fig. 2). In the second geometry, the sample was rotated 90° with respect to the in-plane geometry, with the sample surface close to the vertical plane. For the out-of-plane geometry, $\vec{E}$ is nearly perpendicular to the sample's surface, and the structure is essentially probed along the *c* axis. Two $KTiOPO_4$ (011) single crystals used as a monochromator lead to an energy resolution of approximately 0.5 eV at the Al *K* edge. The spectra were acquired in fluorescence yield (FY) mode under vacuum (10^{-2} mbar) at room temperature.

The Cr $L_{2,3}$ and Cr *K* XANES spectra were probed only for the in-plane geometry on the thin film sample S1. The Cr $L_{2,3}$ edges were recorded at the SOLEIL SR facility on the soft-x-ray beamline SEXTANTS [46]. The spectrum was acquired at room temperature in the total electron yield (TEY) mode, because the FY mode represents only a few percent of the decay process, characteristic for low photon energies such as the Cr $L_{2,3}$ edges (∼570–580 eV), and gives a too weak signal. The Cr *K* edge was recorded on beamline ID12 at the ESRF SR facility [47]. The experiment was performed at low temperature (2.2 K) in FY mode with an x-ray beam incidence lower than 15° from sample S1's surface. The electric field of the x-ray beam was nearly parallel to the film surface, close to the in-plane geometry. The beam size was $100 \times 100\ \mu m^2$, dimensions in the order of magnitude of the grain size.

III. CALCULATION METHODS

A. FEFF

ELNES and XANES spectra recorded at various elemental edges of interest were calculated with the automated multiple scattering (MS) code FEFF 9 [48–50]. The last release (9.6.4), which has a variety of new features and options, is used here. First, there are several new spectroscopies, such as EELS [51], which can now be calculated with FEFF 9. In addition, there is a variety of improvements with respect to the previous version FEFF 8: improved treatments of inelastic losses [52] and of the core-hole interaction [53], as well as more accurate treatment of crystalline systems with *k*-space calculation [54] of the Green's function. FEFF is restricted to the one electron approximation. Moreover, it uses the spherically averaged muffin-tin potentials (MT approximation) that can be a limitation for highly anisotropic materials like *MAX* phases [35]. Throughout this paper, a random-phase approximation (RPA) -screened core hole was selected independently of the scheme used for the calculation [reciprocal (*k*) space or real (*r*) space]. The many-pole model for the self-energy (MPSE card) was considered for treating inelastic loss, the loss function being a weighted average of atomic loss functions (OPCONS card) [55]. For *k*-space calculations presented hereafter, 200 *k* points (kpts) were used to calculate the potentials, and 2000 kpts for the full MS (FMS) calculation (see details in Appendix).

B. WIEN2K

WIEN2K calculations [56] are based on a full-potential band-structure approach. The wave functions (as well as potentials) are described in the whole space using a MT approach consisting of nonoverlapping spheres centered at each atomic site, no assumptions are made in the interstitial region about the shape of the potentials. Inside the MT spheres, the Kohn-Sham equations are solved using a linearized augmented plane wave (LAPW) [57] basis set or an augmented plane wave (APW) basis set combined with local orbitals (APW+lo) [58]. The exchange and correlation were taken into account using the Perdew-Burke-Ernzerhof (PBE) parametrization [59]. As a figure of merit, the total and site-projected DOS of Cr_2AlC are represented in Fig. 3, and are in good agrement with the DFT electronic structure calculations published so far [2,3,6]. The Cr_2AlC valence band reveals both Cr d/C p (from −7 to −3.7 eV) and Cr d/Al p (from −3.1 to −1.6 eV) hybridizations: they denote strong Cr—C bonds and weaker Cr—Al ones, at the origin of most mechanical properties of this nanolaminated compound. At the Fermi level, pure Cr *d* states are dominant, indicating that, in a first approximation, the electronic properties of Cr_2AlC are dominated by the Cr *d* states. Besides its covalent character, Cr_2AlC, like many *MAX* phases [60–62], also presents an ionic component with a charge transfer evidenced by XLD (x-ray linear dichroism) experiment [63] from the Al toward the C, the Cr remaining nearly neutral. The complex nature of this mixture of metallic, covalent and ionic bondings in Cr_2AlC is further emphasized when considering the Cr *d*-*d* electron correlation [64–66], which is responsible of the recently reported Invar-like effect behavior of this compound below 80 K [40].

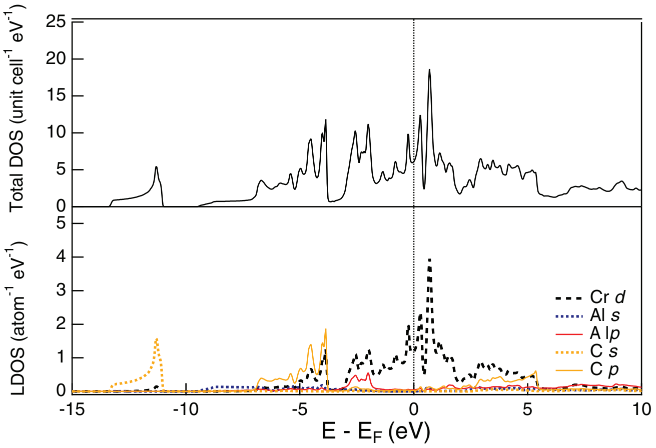

FIG. 3. (Color online) Total (top) and local (bottom) DOS of Cr_2AlC. The Fermi level is indicated by a vertical line.

C. VASP

The Cr_2AlC phonon density of states are obtained using the frozen phonon method. Second-order force constants are calculated from DFT by displacing one atom in a $2 \times 2 \times 1$ supercell. The VASP code [67] was used for this purpose with PAW wave functions and a PBE exchange and correlation function. A plane-wave energy cutoff of 600 eV was used. The $3p$, $3d$, and $4s$ electrons for Cr, the $3s$ and $3p$ electrons for Al, and the $2s$ and $2p$ electrons for C were treated as valence states. The convergence criteria were 10^{-6} eV for the total energy, and 10^{-8} eV for the atomic forces. All inequivalent displacements are considered leading to as many VASP calculations of force constants. Then all force constants are gathered together and Fourier transformed to obtain a dynamical matrix which yields the eigenmodes and eigenenergies by standard solution of the linear system. The PHONOPY software [68] is used for preprocessing prior to use VASP as well as for postprocessing.

IV. RESULTS

A. C *K* edge

The two experimental spectra obtained in $[11\bar{2}0]$ and [0001] zone axes are reported in Fig. 4, after background removal. The slope of both edges is similar, indicating that the preedge background has been removed consistently, and that the normalization procedure (to the intensity of FSs A for the experimental edges here) would not change the interpretation of the differences in FSs arising from the angular dependence. The corresponding k-space theoretical spectra obtained with the FEFF EELS module [54] for an s, p, and d basis set ($l_{\max} = 2$) are also plotted, taking into account all previously quoted experimental parameters (acceleration voltage, convergence and collection angles, electron beam direction, energy resolution). The theoretical spectra have been shifted by -4.55 eV to align FS A with the experimental data to correct the C $1s$ core-level energy calculated by the purely atomic Dirac-Fock code implemented in FEFF [69]. This alignment also accounts for a possible error (typically 1–2 eV) in the determination of the Fermi level in FEFF.

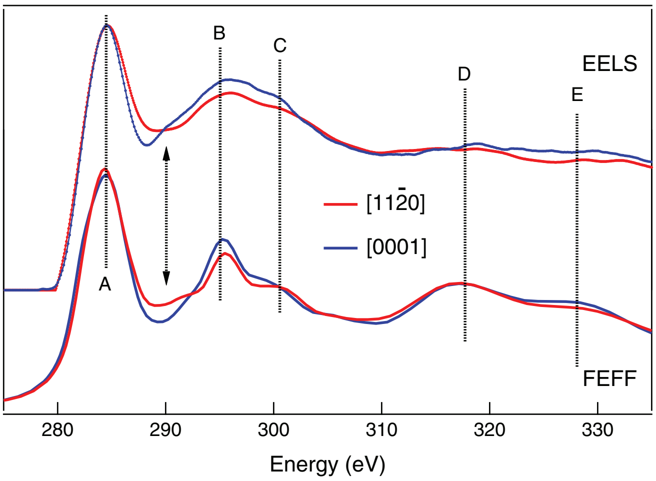

FIG. 4. (Color online) Experimental (top) and calculated (bottom) Cr_2AlC ELNES C *K* edge for the $[11\bar{2}0]$ (red) and [0001] (blue) zone axis. The experimental edges are normalized to the intensity of fine structure A.

Overall, the calculations reproduce the differences observed on the experimental data for the $[11\bar{2}0]$ and [0001] orientations: the minimum (double arrow) between FSs A and B is deeper for [0001] compared to $[11\bar{2}0]$, the FSs B and C have higher intensities for [0001], while FS D appears to be at slightly lower energy for $[11\bar{2}0]$ than for [0001] orientation. Finally, it seems that the intensity magnitude of structure E is smaller for $[11\bar{2}0]$ than [0001], as predicted by the calculation. However, the experimental spectra are much more damped than the calculated ones at high energy, i.e., in the extended energy range (EXELFS), and the amplitude of FS A is too large compared to the experiment. These observed discrepancies can originate from disorder, static or thermal, which is not considered in the present calculation, and a too restricted angular momentum expansion ($l_{\max} = 2$) that has to be increased further away from the edge onset.

Calculating the spectra in r space allows us to decipher the ELNES and to connect some experimental FSs with the Cr_2AlC structure. The decomposition of the C *K* edge among the different coordination shells of near-neighboring (NN) atoms around the central excited C atom is presented in Figs. 5 and 6 for $[11\bar{2}0]$ and [0001] orientations, respectively. To achieve the convergence of the spectra and to match the experiment, a cluster of atoms up to the 17th shell of NN is necessary. Indeed, looking at the calculated spectra prior to the experimental 1.2 eV convolution (dashed line in Figs. 5 and 6), the FS C essentially comes from the 17th atomic layer, which involves six C atoms localized at $c/2$ and six others at $-c/2$. As the FSs can be interpreted as coming from constructive interferences, the FS C conveys a structural order in between C atoms belonging to two octahedra layers located on each side of the layer containing the central C atom, as shown in Fig. 7. Nevertheless, along [0001], this structure is more pronounced in the experiment compared to the calculation. This effect may originate from an anisotropy of disorder in the carbon layers. In addition, except for the six first-nearest-neighbor Al atoms (fourth shell), which contribute to the FS D at 320 eV, the C *K* ELNES is almost insensitive to the Al layers.

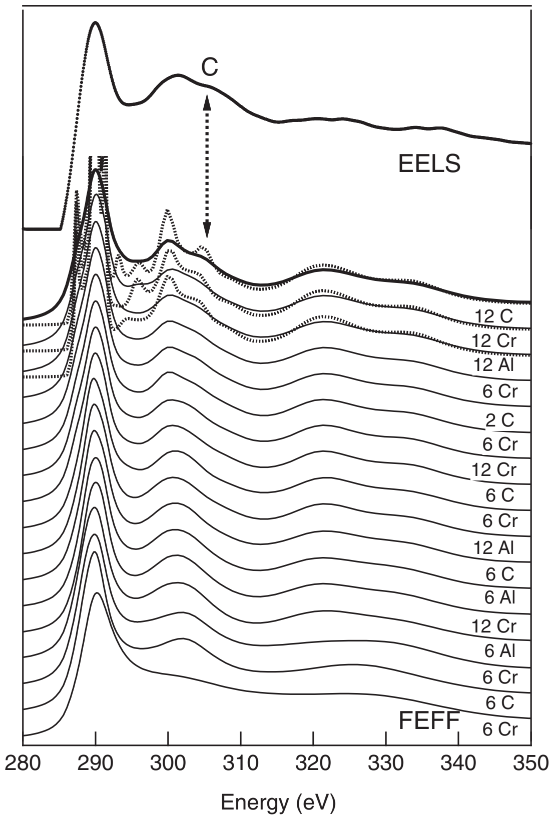

FIG. 5. Decomposition of the Cr_2AlC ELNES C K edge among the different coordination shells for the $[11\bar{2}0]$ (basal plane) zone axis. Dashed lines: clusters involving 15, 16, and 17 shells of atoms before 1.2 eV energy convolution.

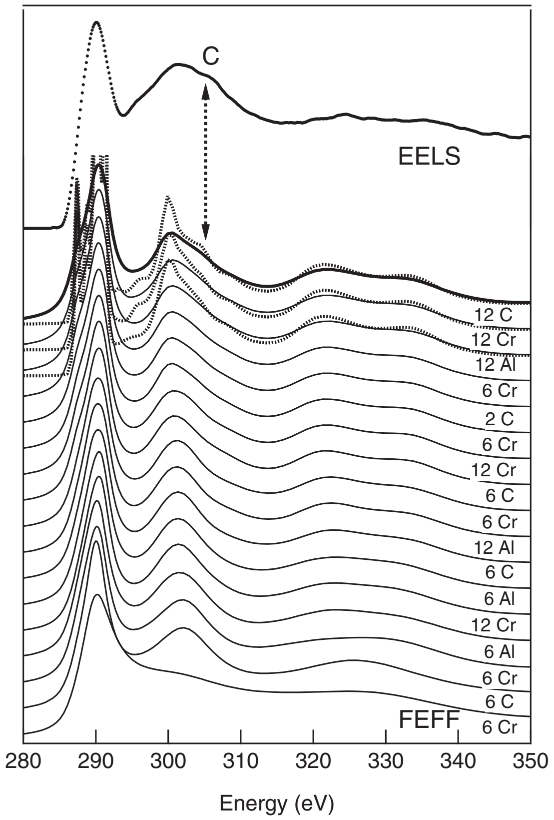

FIG. 6. Decomposition of the Cr_2AlC ELNES C K edge among the different coordination shells for the [0001] (c axis) zone axis. Dashed lines: clusters involving 15, 16, and 17 shells of atoms before 1.2 eV energy convolution.

According to the dipole selection rule, the C K edge reflects the unoccupied projected C p DOS in the material. In Fig. 8, the experimental ELNES spectra recorded along [0001] and $[11\bar{2}0]$ zone axis are compared with C p_{xy} and a weighted average of the C p_z (∼40%) and C p_{xy} (∼60%) calculated empty LDOS obtained from WIEN2K, respectively. These weights were determined according to the scattering geometry [70]. The LDOS were convolved with a Gaussian [full width at half-maximum (FWHM) of 1.2 eV] to account for the experimental energy resolution and the Fermi level was set to 282 eV. The similarities of these LDOS with the experimental and FEFF theoretical spectra are noteworthy: all the experimentally observed FSs correspond to a peak in the LDOS. This result shows that the attractive potential due to the $1s$ core-hole created during the excitation process is negligible at the C K edge in this material, such that the FSs directly reflect the projected density of empty states of p character onto the C atoms. Such a weak effect of the core hole can be understood from the rule given by Mauchamp *et al.* [36], which states that the core hole is important on atoms that significantly participate to the DOS at the Fermi level. From Fig. 3, this is obviously not the case for the carbon atom in Cr_2AlC. Lastly, the anisotropy observed at the C K edge, and thus C p LDOS alike, is very weak because of the octahedral environment of the C atoms, but is nevertheless visible.

B. Al *K* edge

The experimental Al K XANES spectra, recorded for the in-plane and out-of-plane geometries and plotted in Fig. 9, clearly

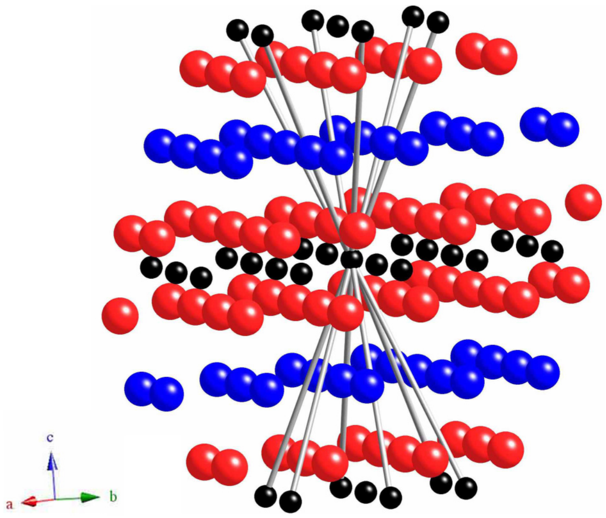

FIG. 7. (Color online) Representation of a cluster of atoms (black: C, red: Cr, blue: Al) up to the 17th shell around a central carbon atom. The 12 carbon atoms at the origin of FS C are linked to the central one by gray lines.

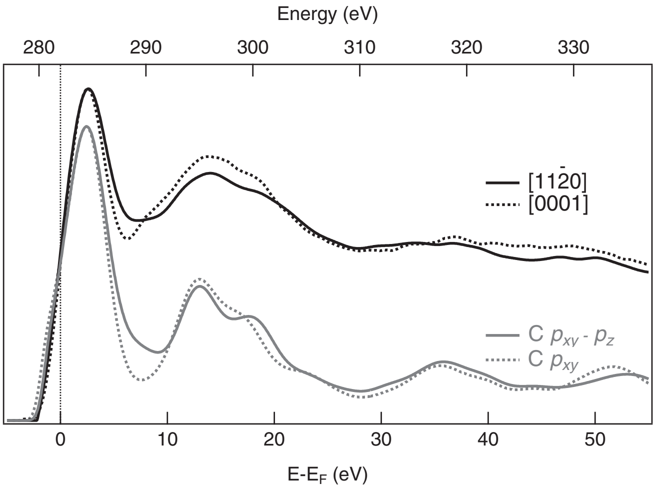

FIG. 8. Comparison of the C K (black) ELNES (top) with the carbon p DOS obtained from WIEN2K calculations (bottom). The experimental edges are normalized to the intensity of fine structure A. The vertical line stands for the Fermi level.

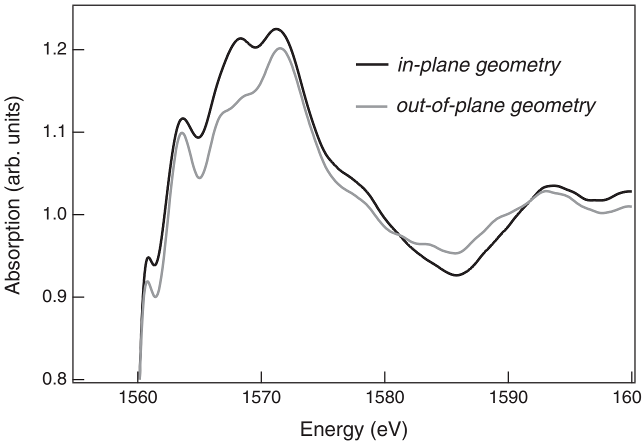

FIG. 9. Experimental Cr$_2$AlC XAS Al K edge for in-plane and out-of-plane geometry.

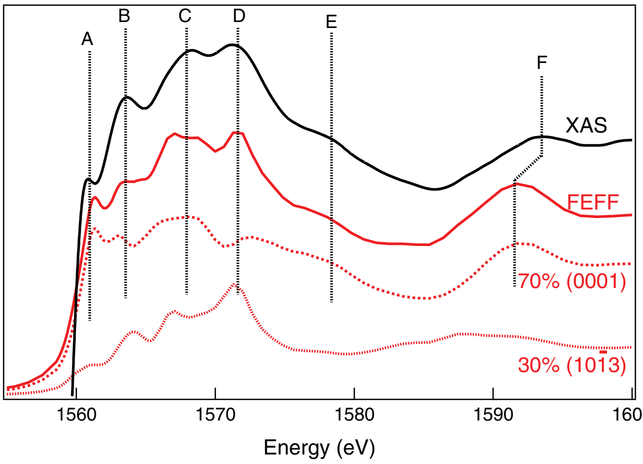

FIG. 10. (Color online) Experimental (black) and calculated (red) Al K XANES for the in-plane geometry. Red dashed and dotted lines are the contributions of the (0001) and (10$\bar{1}$3) planes, respectively.

show the existence of an anisotropy at this edge. The anisotropy results mainly from the asymmetry of charge distribution around an Al atom along the c axis and within the $\{a,b\}$ planes. This effect could be predicted given the fact that each Al atom occupies a trigonal prismatic site, which is less isotropic than the octahedral site occupied by the C atoms. This anisotropy is also predicted by k-space FEFF calculations for both in-plane and out-of-plane geometries. To account for the experimental energy resolution, all FEFF spectra have been convolved with a Gaussian (FWHM of 0.5 eV). First, the in-plane results are shown in Fig. 10, where the experiment is offset for clarity (top). The related FEFF spectrum (bottom: red line) has to be shifted by −5.5 eV to align the maximum at 1571.5 eV (FS D). This spectrum is obtained considering weighted contributions from the (0001) basal planes (70%, dashed red line) and (10$\bar{1}$3) planes (30%, dotted red line). Indeed, the sole consideration of the (0001) planes does not match the experimental XANES shape, and therefore the contribution of the (10$\bar{1}$3) planes that were evidenced from XRD (Fig. 2) must be added. These planes lie at about 60° (Fig. 1) from the basal planes. In that way, all experimentally observed FSs are reproduced by the calculation, where the amplitude and energy position are more or less in agreement. The discrepancy is particularly marked for the first extended fine structure (EXAFS) F observed experimentally at 1593.4 eV while predicted at 1591.7 eV in the calculation. A similar observation has been reported [35] at the Al K edge of Ti$_3$AlC$_2$ and attributed to the muffin-tin approximation, as discussed hereafter.

In the case of the out-of-plane results shown in Fig. 11, the calculated spectrum is obtained considering weighted contributions from the (11$\bar{2}$0) planes (70%, dashed red line), which are perpendicular to the (0001) planes, and the (10$\bar{1}$9) planes (30%, dotted red line), which lie at ∼ 90.27° from the (10$\bar{1}$3) planes. The theoretical spectra have to be shifted by −5.7 eV to align the FS D. Most of the experimental FSs are reproduced by the calculation at the right energy position,

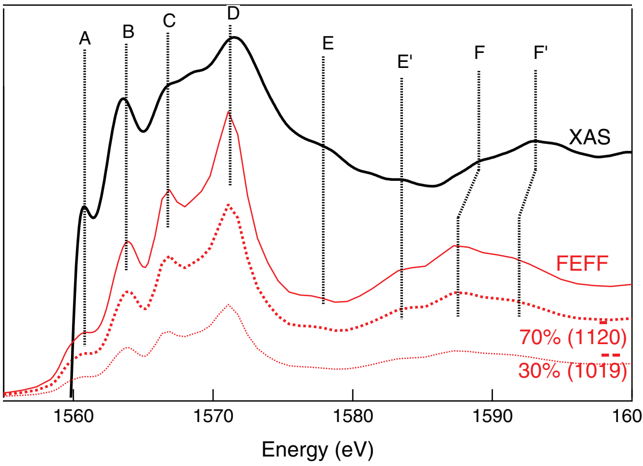

FIG. 11. (Color online) Experimental (black) and calculated (red) Al K XANES for the out-of-plane geometry. Red dashed and dotted lines are the contributions of the (11$\bar{2}$0) and (10$\bar{1}$9) planes, respectively.

except the FS at ~1568 eV in between C and D. Here also, the first EXAFS oscillation (double structure F-F′) is off by about −1.5 eV. Although the shape of the experimental edge from B to D is reproduced overall, the magnitude of the FSs C and D is too high. The reason for this observation could be that, similarly to the C *K* edge, the disorder is not taken into account in the FEFF calculations. From Figs. 10 and 11, it should be noted that the spectra related to the $(11\bar{2}0)$, $(10\bar{1}3)$, and $(10\bar{1}9)$ planes are nearly identical. For this reason, the contribution of the $(10\bar{1}9)$ planes does not modify the calculated XANES significantly for the out-of plane geometry, as compared to the contribution of the $(10\bar{1}3)$ planes for the in-plane geometry. The spherically averaged spectrum, calculated by switching off the polarization control card in FEFF and described in the following, further illustrates this effect.

The spectra calculated without polarization reference in *r* space for clusters of increasing size are plotted in Fig. 12. The XANES is converged for a cluster involving 15 shells of NN atoms (radius: 6.76 Å): all the experimental FSs are reproduced by the calculation. This *r*-space spectrum is nearly identical to the *k* space one obtained for the in-plane geometry, i.e., when adding about 70% of the basal planes and 30% of the pyramidal planes response (see Fig. 10). The main difference concerns the shape of the FS C, which is double for the calculation in *k* space while it is single for the one in *r* space and for the experiment. Using different energy shifts for the $(10\bar{1}3)$ and (0001) contributions before adding them allows to suppress this double structure. Different energy shifts may correspond to potentials that are different in the $\{a,b\}$ planes and along the *c* axis, i.e., nonspherical potentials, opposite to the muffin-tin ones used in FEFF. Nevertheless, this discrepancy remains minor, and the *r*-space shell-by-shell decomposition is a reliable method to link experimental FSs to the environment of the Al atomic surroundings in Cr_2AlC. For example, FSs A and D start to appear with the third shell (6 C at $\pm c/4$) and their magnitude increase when including the fourth shell (6 Cr at 3.92 Å). FSs C and E mainly originate from the seventh shell involving 12 Cr at $\pm c/6$, atoms belonging to Cr layers on each side of the Al layer, which includes the excited Al atom considered. Finally, the FS B is reproduced when considering the 15th shell of 12 C located at $\pm c/2$. Thus, similarly to the C *K* ELNES, the Al *K* XANES allows us to probe the Cr_2AlC structure up to $\pm c/2$, i.e., a whole unit cell length.

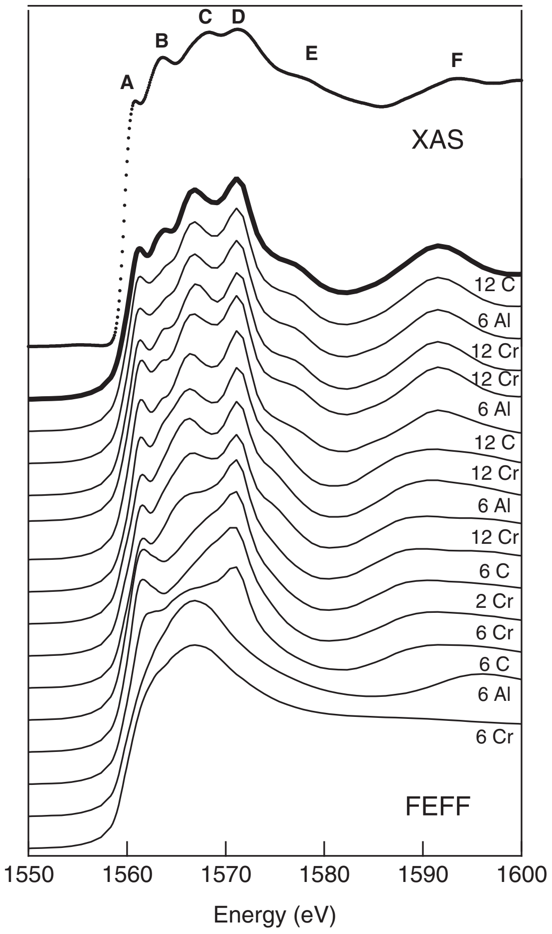

FIG. 12. Decomposition among the different coordination shells of the spherically averaged (unpolarized) FEFF Al *K* XANES. Thick black line: fully converged spectrum involving 15 shells of NN atoms. Top: XAS spectrum recorded for the in-plane geometry.

Due to the dipole selection rules, the anisotropy of the Al *p* states evidenced from polarized XAS spectra can also be compared to the Al *p* DOS. It is not possible to get such information from the FEFF code because the LDOS are related to muffin-tin potentials, i.e., they are spherically averaged. However, WIEN2K allows such a comparison as it is a full-potential code. This approach is illustrated in Fig. 13 for each geometry (top: in-plane, bottom: out-of-plane). The basal planes description is performed by considering the Al p_{xy} DOS while the Al p_z DOS is used to describe the structure along the *c* axis. The LDOS have been broadened with a Gaussian (FWHM of 0.5 eV) to account for the experimental energy resolution and the energy reference for the Fermi level is taken at the inflection point (1559 eV: first derivative maximum) of the experimental data. The XAS spectra calculated with WIEN2K, without considering a core hole, are also shown (dashed lines). These two spectra are closely related to the corresponding LDOS and are very similar to those obtained with FEFF for the (0001) and $(11\bar{2}0)$ planes (red dashed lines in Figs. 10 and 11). Here also, it is clear that the calculated XANES does not match the experiment for the in-plane geometry if only the basal plane contribution is considered (Fig. 13, top). A contribution of the $(10\bar{1}3)$ planes, whose spectrum has been shown to be very similar in shape to the one obtained for the out-of-plane geometry (Fig. 13, bottom) should be considered. The agreement with the experiment observed for the energy position of the first EXAFS FS F is noteworthy, and confirms that the FEFF discrepancies mentioned above (Figs. 10 and 11) originate from the muffin-tin approximation.

C. Cr $L_{2,3}$ edges

Although the standard one-electron model fails at describing soft-x-ray edges for early 3*d* transition metals such as Cr [71,72], the Cr $L_{2,3}$ edges are calculated here using FEFF in an attempt to reproduce the experimental FSs. The experimental spectrum plotted in Fig. 14 shows that the $L_{2,3}$ edges are very different from those of metallic Cr, which only show white lines without any fine structure [73]. A double

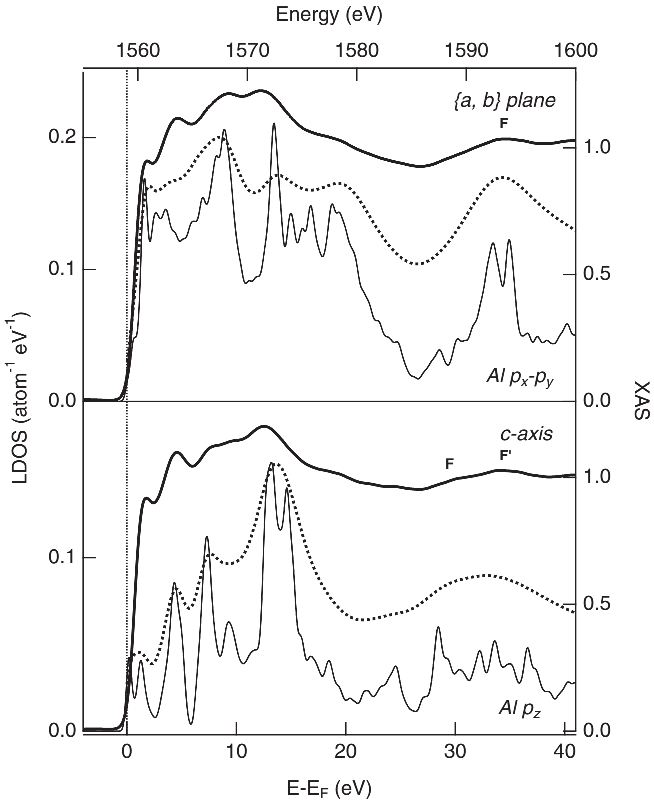

FIG. 13. Comparison of the Al K XAS (full lines, thick) with Al p DOS (full lines, thin) and XAS spectra (dashed lines) obtained from WIEN2K calculations. Top: in-plane geometry (basal plane), bottom: out-of-plane geometry (c axis). The vertical line stands for the Fermi level.

structure is visible at the top of both L_3 and L_2 edges, with a clearer splitting at the L_3 as compared to the L_2 (energy separation: ~1.1 eV). Their relative intensities are inverted when going from L_3 to L_2.

Two different FEFF calculations were performed: the first one includes a core hole while the second only considers the ground state (i.e., no core hole). From the criterion evoked by Mauchamp *et al.* [36], the Cr_2AlC ground-state density of states at the Fermi level is dominated by the Cr d states (Fig. 3), and a significant core-hole effect is expected at the Cr edges. The same criterion predicts an opposite behavior at the C K and Al K edges, in agreement with what was previously mentioned in Secs. IV A and IV B. The FEFF calculations shown in Fig. 14 support this prediction: considering the core hole (red full line) leads to a lower intensity as compared to the ground-state result (red dashed line), an effect related to the core-hole screening that partly fills the empty Cr d states. These calculated spectra account for the $2p_{3/2,1/2}$ spin-orbit splitting, which was measured to 9 eV, while the calculated value from FEFF is 10 eV. Thus 1 eV must be subtracted from the L_2 edge energy scale, before placing the L_3 and L_2 contributions on the same energy grid and adding them. Finally, the calculated spectra have to be shifted by -7.6 eV to correct the purely atomic Cr $2p_{1/2}$ and $2p_{3/2}$ core-level energies. Both calculations predict the experimental double structure observed at the top of the L_3 and L_2 edges, however the relative intensities of the double structure are inverted at the L_3 edge, while the double structure is too pronounced at the L_2 edge, which is too broad as compared to the experiment. Furthermore, the calculated L_3/L_2 "branching ratio" is close to 2, in agreement with the predicted value from the independent-electron approximation, while the experimental "branching ratio" is closer to unity. It is worth noting that for an RPA core hole, FEFF nearly agrees with the experimental L_2 intensity, and strongly underestimates the L_3 one, whereas it is the opposite for the ground-state approach. For the experimental geometry used here, the electric field $\overrightarrow{E}$ of the incident x-ray beam is parallel to the sample's surface consisting mainly of Cr_2AlC basal planes. In that case, XAS measurements mainly probe the unoccupied Cr $3d_{xy}$ and $3d_{x^2-y^2}$ in-plane orbitals, the x-y projection of the $3d_{xz}$ and $3d_{yz}$ orbitals, but also a much smaller $p \rightarrow s$ contribution. These partial LDOS are obtained from WIEN2K after convolution with a Gaussian function (FWHM of 0.5 eV), and are shown in Fig. 15, the Fermi level being set at the experimental L_3 (572.6 eV) threshold. The LDOS does not include the core-hole effect that will modify the relative

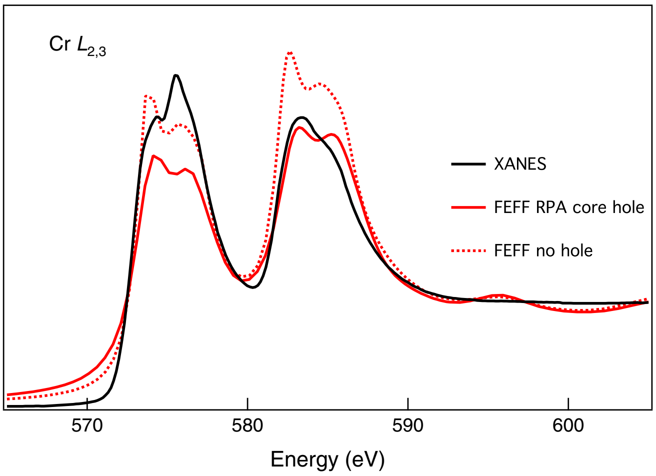

FIG. 14. (Color online) Comparison of the Cr $L_{2,3}$ XAS (black) with spectra obtained from FEFF calculations with (red line) and without (red dashes) a core hole.

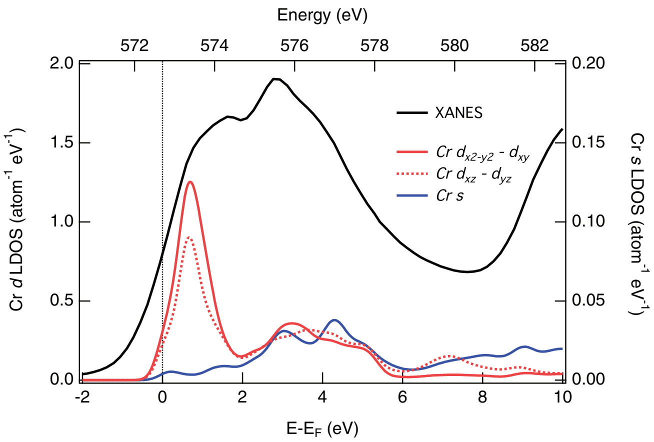

FIG. 15. (Color online) Comparison of the Cr L_3 XAS (black) with d (red) and s (blue) LDOS obtained from WIEN2K calculations. The vertical line stands for the Fermi level.

intensities of the DOS components because its consideration needs to use a supercell, whose size is quite large for *MAX* phases. Therefore, these LDOSs are only qualitative, but they have the merit of supporting the experimental FSs. In particular, the shoulder observed just above 576 eV is assignable to the $p \rightarrow s$ transition. A more appropriate method for describing the $L_{2,3}$ edges is a fully atomic approach, including the crystal or ligand field, because the strongly localized core hole has larger dipole matrix element with atomiclike rather than with bandlike wave functions. Unfortunately, Cr is not in a cubic symmetry in Cr_2AlC (the Cr point-group symmetry is $3m$), thereby complicating the use of the multiplet theory [74–76]. Despite recent encouraging progress in this field [71], these observations outline that the theoretical description of the *M* element *L* edges in *MAX* phases is still challenging.

D. Cr *K* edge

The FEFF calculations were performed in *k* space with an *s*-*p*-*d*-*f* basis set ($l_{\max} = 3$), and the spectra related to the (0001) and (10$\bar{1}$3) planes are plotted in Fig. 16 (bottom) in addition to the experimental spectrum. The calculations are aligned on the experimental FS B (5993.4 eV), which is required to correct the calculated Cr 1*s* energy level. The value of the energy shift for the (0001) spectrum is $\Delta E = -6.6$ and -7.6 eV for the (10$\bar{1}$3) spectrum. The overall shape of the experimental data and the (0001) calculated spectrum look similar but several differences exist: the relative intensities of the FSs D and E are inverted as compared with the experiment, while the shoulder A at the bottom of the edge onset is entirely missing. The agreement between the experiment and the calculations greatly improves when the measured signal is considered as a linear combination of basal plane and (10$\bar{1}$3) contributions, as in the case of the Al *K* edge. The results obtained by considering contributions for the (0001) planes as 70% (red), 60% (dark blue), and 50% (light blue) of the measured signal are plotted on the same figure. Interestingly, the shoulder A becomes more prominent as the weight of the (10$\bar{1}$3) contribution increases.

All experimentally observable FSs are reproduced by the calculation for the 50-50 combination: the linear shape of the experiment just after the FS C is nicely reproduced as well as the relative amplitude of the FSs D and C, even if the intensity of the FS D is slightly underestimated in the calculation. The only discrepancy is at energies higher than 6050 eV, i.e., at the beginning of the first EXAFS oscillation, whose amplitude is too high. Here also, this effect can be related to structural disorder that is not considered up to now. Furthermore, it is difficult to firmly consider that the measured data correspond to a 50-50 or 60-40 mixture of (0001) and (10$\bar{1}$3) contributions. However, it must be mentioned that this result does not signify that sample S1 is constituted of an equal, or roughly equal, distribution of (0001) and (10$\bar{1}$3) grains. Due to the small beam size, half of the illuminated sample area is (0001) oriented while the second half is (10$\bar{1}$3) oriented. This analysis is far different from what is obtained at the Al *K* edge for sample S2 [70% (0001), 30% (10$\bar{1}$3)] because in that latter case, the data are acquired in grazing incidence with a larger beam so that the whole surface is illuminated by the incident x-ray beam: the measured signal is thus representative of the whole sample. The use of different energy shifts for (0001) and (10$\bar{1}$3) planes has a visible effect at the Cr *K* edge onset, as illustrated in Fig. 17, which is an expanded plot of Fig. 16 in the vicinity of FSs A and B. The reproduction of these FSs is emphasized when $\Delta E = -6.6$ eV for the (0001) spectrum, and $\Delta E = -7.6$ eV for the (10$\bar{1}$3) spectrum. However, if $\Delta E = -6.6$ eV is used for both spectra, as it must be from principle, it leads to a very poor agreement with the experiment close to the edge onset (dotted lines): the FS B is off by about 2 eV, while FS A, as mentioned above, is entirely missing. The only physical justification to apply different energy shifts for (0001) and (10$\bar{1}$3) spectra before adding them is related to the muffin-tin approximation, such that different energy shifts provide a way to compensate for nonspherical potential effects, as verified from WIEN2K full-potential calculations. Finally,

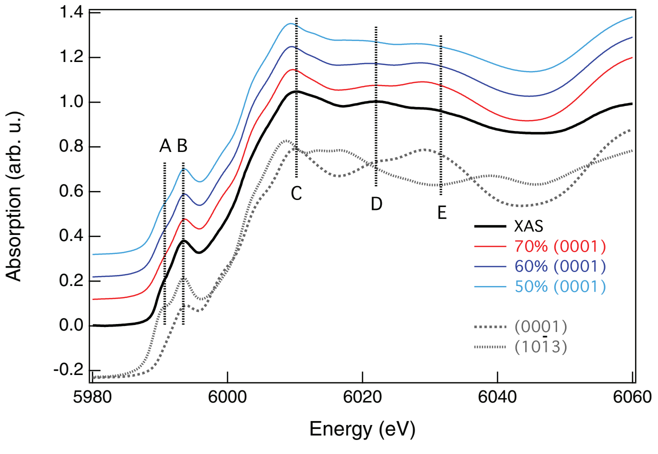

FIG. 16. (Color online) Experimental (black) and calculated [gray dashes: (0001) planes, gray dots: (10$\bar{1}$3) planes] Cr *K* XANES. Also shown are linear combinations for x% of (0001) and 100-x% of (10$\bar{1}$3) contributions for $x = 70$ (red), 60 (dark blue), and 50 (light blue). The spectra are offset for clarity.

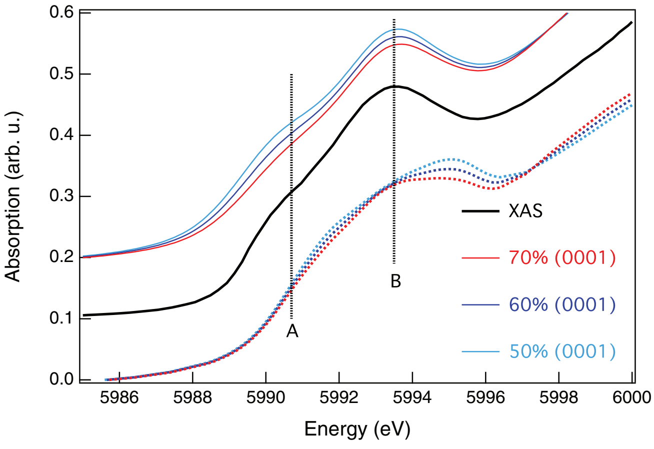

FIG. 17. (Color online) Expanded view of the spectra plotted in Fig. 16 at the edge onset. Dotted lines are results using $\Delta E = -6.6$ eV for both (0001) and (10$\bar{1}$3) contributions. The spectra are offset for clarity.

it should be emphasized that the quadrupole contributions were not included in the calculations. Nevertheless, the overall agreement between experimental and calculated FSs A and B at the edge onset suggests that the dipolar approximation allows us to correctly interpret the Cr *K* XANES.

V. DISCUSSION

Several authors have reported the importance of Cr *d-d* electron correlation in Cr_2AlC [64–66] and Cr_2GeC [61,77] to accurately describe their structural and mechanical properties. To overcome this difficulty, experimental lattice parameters were chosen for the calculations of near-edge structures in the present study (see Sec. II A 1). The energy and intensity of most FSs in the experimental C *K* ELNES, and Al *K* and Cr *K* XANES, are well reproduced from first-principles calculations. This observation infers that the electronic correlation effects in the Cr *d* band, which were not taken into account in the present calculations, have a weak influence on the *p* states probed at the *K* edges. This can be related to the fact that, in a first approximation, *d* states are not probed. These results are in agreement with the calculation of Cr_2AlC plasmon excitation, whose accurate description does not require considering the electron correlation effects [28].

The investigation of the spectral shapes of C *K* and Al *K* edges employing angular-dependent EELS and XAS shed light on the anisotropy of the Cr_2AlC electronic structure. The most salient points are the nearly isotropic character of the C site and the marked anisotropy of the Al site. It mainly reflects the symmetry in each atomic site, the C site being of higher symmetry than the Al one. It should be mentioned that a similar difference is predicted by theoretical calculations concerning the charge states of C and Al in this *MAX* phase. In Table I are reported the charge configurations per atom obtained from FEFF at the end of the self-consistent loop. As mentioned in Sec. III, a charge transfer occurs from Al toward C, with Cr remaining nearly neutral, a result in qualitative agreement with the calculation using the orthogonalized linear combination of atomic orbitals method [62]. The consequence of this effect is a charge modulation along the *c* axis, which reflects the chemical modulation along this direction that is interlocked with the anisotropy.

The structure anisotropy of Cr_2AlC has also consequences on its vibrational density of states (VDOS) and thus its thermal properties. The thermal expansion coefficients are different in the basal plane and along the *c* axis [40,78]. The VDOS are plotted in Fig. 18.

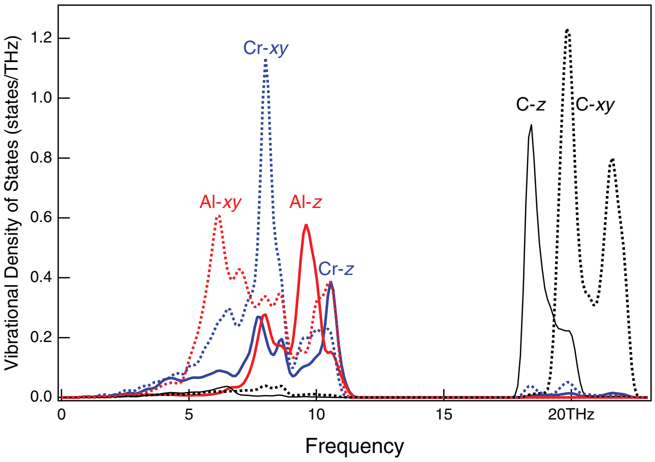

FIG. 18. (Color online) Cr_2AlC phonon partial density of states. Full lines: *c*-axis vibrations, dotted lines: basal-plane vibrations.

TABLE I. Summary of charge configuration per atom in Cr_2AlC from FEFF.

	Core	Valence (electron unit)	Total charge (electron unit)	Charge transfer (electron unit)
Cr	Mg	$s^{0.477}\ p^{6.758}\ d^{4.78}$	24.015	+0.015
Al	Ne	$s^{0.887}\ p^{1.141}\ d^{0.293}$	12.304	− 0.679
C	He	$s^{1.469}\ p^{2.936}\ d^{0.248}$	6.653	+0.653

The lowest-energy vibrations are associated with the Al atoms in Cr_2AlC, similarly to Ti_3AC_2 (A = Si, Al, and Ge) for which Togo *et al.* found that the lowest-energy vibrations are from the *A* element [79]. Furthermore, vibrations of the Al layers along the basal planes occur at lower energies than those along the *c* axis. The same trends exist for Cr atoms, but at slightly higher energies. The C atoms vibrations take place at the highest energies, a conclusion in agreement with the fact that the Cr—C bonds are the stiffest. Finally, the Al and Cr vibrations appear to be correlated, especially along the *c* axis. Phonons have in turn consequences on core-level spectra as soon as the temperature departs from 0 K during data collection. Indeed, as mentioned previously, all the FEFF calculations presented in Sec. IV do not include any disorder, i.e., they are relative to a perfect structure at 0 K. Yet, the agreement between experimental and calculated spectra worsens for energies at about 30–40 eV above the threshold, i.e., in the EXAFS range. From the VDOS analysis, it is reasonable to use the correlated Debye-Waller model implemented in FEFF to account for thermal disorder in *MAX* phases once the Debye temperature Θ_D is known. For Cr_2AlC, the Debye temperature value calculated from the mean sound velocity is used ($\Theta_D = 644$ K) [80]. However, the thermal disorder is not the only kind of disorder to consider: a static disorder may also exist, resulting from several effects such as defects (vacancies, interstitials, stacking faults, twins, etc.), and residual stress, which are common during thin-film growth. In the FEFF framework, a static disorder can be taken into account by adding a global Debye-Waller factor using the SIG2 control card, allowing for the separate study of the effects of these two different kinds of disorder by considering the Cr and Al *K* edges. Indeed, at a recording temperature of 2.2 K, the thermal disorder at the Cr *K* edge can be neglected without any doubt while its effect can be considered at the Al *K* edge recorded at room temperature (300 K). The primary interest is thus to know if it is possible to estimate the disorder and its nature (static or thermal) in the XANES range. To achieve this goal, unpolarized Cr and Al *K* theoretical spectra that are close to experimental data for the in-plane geometry were calculated, as shown in Fig. 19. First, in the case of the Cr *K* edge (top in Fig. 19), a static disorder σ^2 of magnitude 0.01 Å^2 affects the shape of the spectrum only above 6050 eV, i.e., more

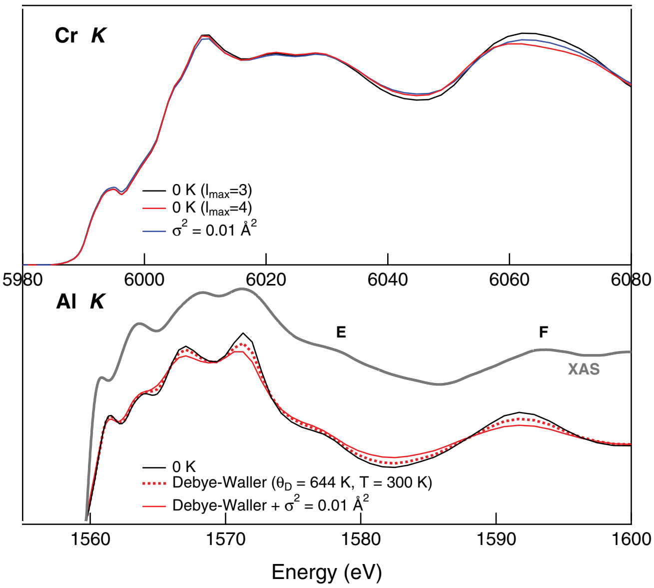

FIG. 19. (Color online) Top: effect of a static disorder and basis-set size at the Cr K edge. Bottom: effect of the thermal (Debye-Waller) and static disorder at the Al K edge.

than 50 eV above the threshold, in the extended energy range (EXAFS). This point is confirmed by the fact that considering a basis set including g states ($l_{\max} = 4$) has a stronger effect on the magnitude of EXAFS oscillation observed at 6065 eV than a static disorder of 0.01 Å^2. The well-known theoretical point where the extended energy range description needs to use a large angular momentum basis is reached ($l_{\max} = 20$ for EXAFS calculations with FEFF). The static disorder does not have a significant contribution in the XANES range, and therefore a reliable estimate of its order of magnitude from the Cr K edge cannot be obtained. Secondly, the thermal disorder improves the agreement between the experiment and the calculation at the Al K edge (bottom in Fig. 19). In particular, the relative intensities of the FSs E and F, which have the same magnitude in the experiment (gray line in Fig. 19), become closer to each other. However, the intensity of the FS F remains too high as compared to E. Adding a static disorder of magnitude $\sigma^2 = 0.01$ Å^2 globally improves the agreement with the experiment. The EXAFS oscillation F is not at the experimentally observed energy position, therefore the static disorder is hardly quantitative from the XANES alone (0.01 Å^2 is too large). A quantitative determination of the disorder around Al atoms would require additional experiments such as EXAFS at various temperatures in order to disentangle the static and thermal disorders. Nevertheless, these results demonstrate that a static component exists for the disorder in the Cr_2AlC thin films studied that is likely related to residual stress and/or defects inherent to the sputtering deposition process.

VI. CONCLUSION

The electronic structure anisotropy of Cr_2AlC has been investigated by comparing core-level spectra obtained from EELS and XAS experiments with *ab initio* FEFF and DFT calculations. The calculations reproduce most of the experimental spectra on the full energy range probed, without considering the Cr d-d electron correlation. The analysis of the C K ELNES provides information about the atomic arrangement around the excited atom through the sensitivity of FSs to C atoms belonging to different Cr_2C octahedra layers. The anisotropy of the C site is weak, as opposed to the Al site. The simulations of the polarization-dependent Al K edge XANES data related to the sputtered thin-film sample S2 show that this film is composed of 70% (0001)- and 30% $(10\bar{1}3)$-oriented grains. A significant anisotropy of the Al p DOS is also evidenced in the basal planes and along the c axis. Furthermore, the near-neighboring atoms shell-by-shell analysis of the data demonstrates that the Al K XANES is sensitive to the local atomic arrangement in Cr_2AlC up to $\pm c/2$. The study of the sputtered thin-film sample S1 at the Cr K edge reveals that the very small probe size and high photon flux available now at SR facilities combined with the latest version of FEFF can be a very powerful tool for material science. A subtle analysis of the FSs at the edge onset allows for an estimate at ±10% of the (0001) and $(10\bar{1}3)$ contributions for a probed area of 100×100 μm^2. It also appears that the PVD-grown thin films have some static disorder, which is likely related to the process of growth. Precisely quantifying the disorder from the ELNES and XANES simulations, however, remains a difficult task given the inherently limited bandwidth. Furthermore, it is worth emphasizing that the theoretical description of the Cr_2AlC anisotropy is not an ideal case for the FEFF code, given the spherical geometry of the potentials. Although the one-electron and muffin-tin approximations are thought to be too restrictive for describing anisotropic materials such as *MAX* phases, the overall agreement between the experimental and calculated spectra outlines the success of FEFF for analyzing such complex materials. This study demonstrates that EELS and XAS results are consistent with those predicted from DFT calculations, and that the current theoretical description and understanding of the electronic structure of *MAX* phases allows for an accurate interpretation of excited states from EELS and XAS.

ACKNOWLEDGMENTS

M.B. and V.M. thank A.-M. Flank and P. Lagarde for assistance and help during the XAS experiments, and the SOLEIL synchrotron facility for funding and access to the LUCIA beamline. The authors are grateful to N. Jaouen (SOLEIL) and A. Rogalev (ESRF) for measuring Cr $L_{2,3}$ and K edges and for their useful comments, Philippe Guérin (Institut Pprime) for technical assistance during thin-film deposition, and P. Chartier (Institut Pprime) for providing the bulk Cr_2AlC sample.

APPENDIX

In this appendix, we describe the way to select the number of k points (kpts) used for the k-space calculations presented in this paper. Due to the large anisotropy and volume of the unit cell (Fig. 1), the calculation proceeds in two steps. The first one, the calculation of the potentials, is the most time-consuming because it involves a SCF loop. Due to the unit cell size, the convergence is achieved with a relatively small size in reciprocal space. Then the mesh of k vectors used to sample the Brillouin zone (BZ) has to be specified, either

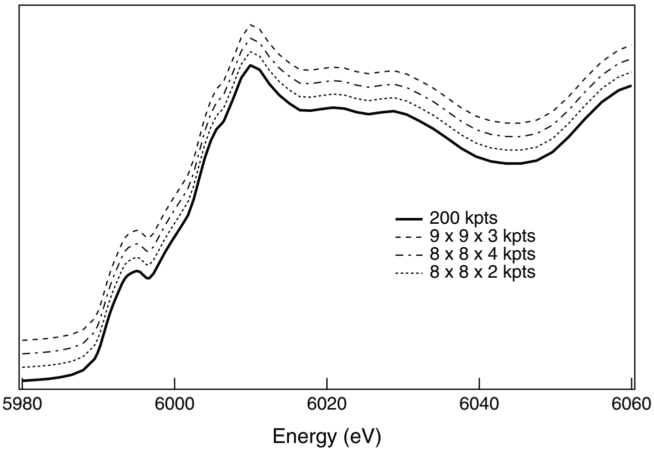

FIG. 20. Cr K edge spectra obtained asking for various number of kpts during the potential calculation. In each case, multiple-scattering calculation is asking for 2000 kpts. The bold line corresponds to the choice selected throughout this paper.

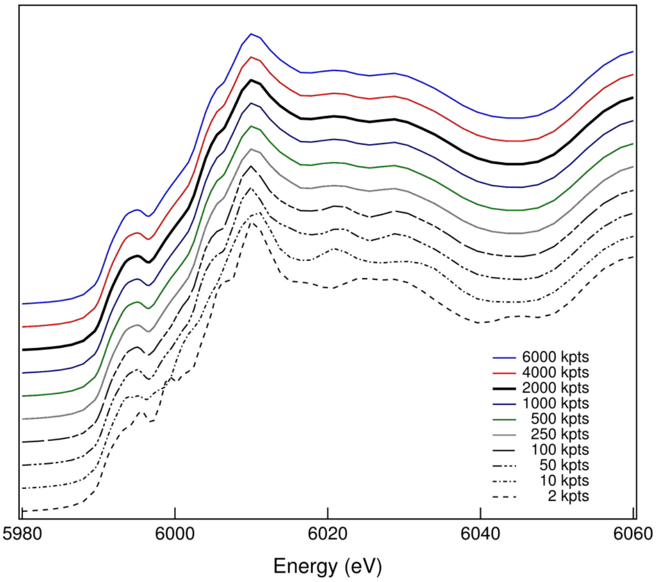

FIG. 21. (Color online) Cr K edge spectra obtained using different k-point meshes for the multiple-scattering calculation. In each case, potentials are calculated asking for 200 kpts. Converged spectra are denoted by full lines. The bold line corresponds to the choice selected throughout this paper.

as the total number or as the detailed k mesh along k_x, k_y, and k_z. The results obtained selecting just 200 kpts or various combinations of k_x, k_y, and k_z ($9 \times 9 \times 3$, $8 \times 8 \times 4$, and $8 \times 8 \times 2$) are shown in Fig. 20 for the unpolarized Cr K edge as example. For all cases, 2000 kpts are then used to calculate the corresponding XANES spectrum. The spectra displayed in Fig. 20 are evidently identical.

The second step is to select the number of kpts used to perform the multiple-scattering calculation. The spectra obtained for various numbers of kpts are shown in Fig. 21 (from top to bottom: 6000, 4000, 2000, 1000, 500, 250, 100, 50, 10, and 2), the number for the potentials being fixed to 200. The convergence is reached for about 250 kpts. To ensure a full convergence of the spectrum, all simulations presented in this paper are performed with 2000 kpts (corresponding to 1764 kpts in the full BZ) for the multiple-scattering calculation and 200 kpts (corresponding to 100 kpts in the full BZ) for the potentials determination.

[1] W. Jeitschko, H. Nowotny, and F. Benesovsky, Monatsh. Chem. **94**, 1198 (1963).

[2] Z. Sun, D. Music, R. Ahuja, S. Li, and J. M. Schneider, Phys. Rev. B **70**, 092102 (2004).

[3] J. M. Schneider, Z. Sun, R. Mertens, F. Uestel, and R. Ahuja, Solid State Commun. **130**, 445 (2004).

[4] Z. Lin, M. Zhuo, Y. Zhou, M. Li, and J. Wang, J. Appl. Phys. **99**, 076109 (2006).

[5] Z. Lin, Y. Zhou, and M. Li, J. Mater. Sci. Technol. **23**, 721 (2007).

[6] G. Jia and L. Yang, Physica B **2405**, 4561 (2010).

[7] Q. M. Wang, A. Flores Renteria, O. Schroeter, R. Mykhaylonka, C. Leyens, W. Garkas, and M. to Baben, Surf. Coat. Technol. **204**, 2343 (2010).

[8] Z. Lin, M. Li, J. Wang, and Y. Zhou, Acta Mater. **55**, 6182 (2007).

[9] D. B. Lee and T. D. Nguyen, J. Alloys Compounds **464**, 434 (2008).

[10] V. D. Jovic, B. M. Jovic, S. Gupta, T. El-Raghy, and M. W. Barsoum, Corrosion Sci. **48**, 4274 (2007).

[11] W. B. Tian, P. Wang, Y. Kan, and G. Zhang, J. Mater. Sci. **43**, 2785 (2008).

[12] J. M. Schneider, D. P. Sigumonrong, D. Music, C. Walter, J. Emmerlich, R. Iskandar, and J. Mayer, Scr. Mater. **57**, 1137 (2007).

[13] Z. Sun, S. Li, R. Ahuja, and J. M. Schneider, Solid State Commun. **129**, 589 (2004).

[14] J. Wang and Y. Zhou, Phys. Rev. B **69**, 214111 (2004).

[15] J. Emmerlich, D. Music, A. Houben, R. Dronskowski, and J. M. Schneider, Phys. Rev. B **76**, 224111 (2007).

[16] M. W. Barsoum, *MAX Phases* (Wiley-VCH, Weinheim, 2013).

[17] M. W. Barsoum, Prog. Solid State Chem. **28**, 201 (2000).

[18] Z. Lin, M. Li, and Y. Zhou, J. Mater. Sci. Technol. **23**, 145 (2007).

[19] J. Wang and Y. Zhou, Annu. Rev. Mater. Res. **39**, 415 (2009).

[20] H.-I. Yoo, M. W. Barsoum, and T. El-Raghy, Nature (London) **407**, 581 (2000).

[21] L. Chaput, G. Hug, P. Pécheur, and H. Scherrer, Phys. Rev. B **71**, 121104(R) (2005).

[22] T. Scabarozi, A. Ganguly, J. D. Hettinger, S. E. Lofland, S. Amini, P. Finkel, T. El-Raghy, and W. Barsoumm, J. Appl. Phys. **104**, 073713 (2008).

[23] P. Eklund, M. Bugnet, V. Mauchamp, S. Dubois, C. Tromas, J. Jensen, L. Piraux, L. Gence, M. Jaouen, and T. Cabioc'h, Phys. Rev. B **84**, 075424 (2011).

[24] V. Mauchamp, W. Yu, L. Gence, L. Piraux, T. Cabioc'h, V. Gauthier, P. Eklund, and S. Dubois, Phys. Rev. B **87**, 235105 (2013).

[25] N. Haddad, E. Garcia-Caurel, L. Hultman, M. W. Barsoum, and G. Hug, J. Appl. Phys. **104**, 023531 (2008).

[26] G. Hug, P. Eklund, and A. Orchowski, Ultramicroscopy **110**, 1054 (2010).
[27] V. Mauchamp, G. Hug, M. Bugnet, T. Cabioc'h, and M. Jaouen, Phys. Rev. B **81**, 035109 (2010).
[28] V. Mauchamp, M. Bugnet, P. Chartier, T. Cabioc'h, M. Jaouen, J. Vinson, K. Jorissen, and J. J. Rehr, Phys. Rev. B **86**, 125109 (2012).
[29] M. Magnuson, O. Wilhelmsson, J.-P. Palmquist, U. Jansson, M. Mattesini, S. Li, R. Ahuja, and O. Eriksson, Phys. Rev. B **74**, 195108 (2006).
[30] M. Magnuson, M. Mattesini, S. Li, C. Höglund, M. Beckers, L. Hultman, and O. Eriksson, Phys. Rev. B **76**, 195127 (2007).
[31] M. Magnuson, M. Mattesini, O. Wilhelmsson, J. Emmerlich, J.-P. Palmquist, S. Li, R. Ahuja, L. Hultman, O. Eriksson, and U. Jansson, Phys. Rev. B **74**, 205102 (2006).
[32] M. Magnuson, J.-P. Palmquist, M. Mattesini, S. Li, R. Ahuja, O. Eriksson, J. Emmerlich, O. Wilhelmsson, P. Eklund, H. Högberg, L. Hultman, and U. Jansson, Phys. Rev. B **72**, 245101 (2005).
[33] M. Magnuson, O. Wilhelmsson, M. Mattesini, S. Li, R. Ahuja, O. Eriksson, H. Högberg, L. Hultman, and U. Jansson, Phys. Rev. B **78**, 035117 (2008).
[34] M. Magnuson, M. Mattesini, N. V. Nong, P. Eklund, and L. Hultman, Phys. Rev. B **85**, 195134 (2012).
[35] M. Bugnet, V. Mauchamp, P. Eklund, M. Jaouen, and T. Cabioc'h, Acta Mater. **61**, 7348 (2013).
[36] V. Mauchamp, M. Jaouen, and P. Schattschneider, Phys. Rev. B. **79**, 235106 (2009).
[37] T. Ouisse, E. Sarigiannidou, O. Chaix-Pluchery, H. Roussel, D. Doisneau, and D. Chaussende, J. Cryst. Growth **384**, 88 (2013).
[38] P. Eklund, M. Beckers, U. Jansson, H. Högberg, and L. Hultman, Thin Solid Films **518**, 1851 (2010).
[39] J. Etzkorn, M. Ade, and H. Hillebrecht, Inorg. Chem. **46**, 7646 (2007).
[40] M. Jaouen, P. Chartier, T. Cabioc'h, V. Mauchamp, G. André, and M. Viret, J. Am. Cer. Soc. **96**, 3872 (2013).
[41] V. J. Keast, S. Harris, and D. K. Smith, Phys. Rev. B **80**, 214113 (2009).
[42] G. Abadias, L. E. Koutsokeras, Ph. Guérin, and P. Patsalas, Thin Solid Films **518**, 1532 (2009).
[43] R. F. Egerton, Rep. Prog. Phys. **72**, 016502 (2009).
[44] A.-M. Flank, G. Cauchon, P. Lagarde, S. Bac, M. Janousch, R. Wetter, J.-M. Dubuisson, M. Idir, F. Langlois, T. Moreno, and D. Vantelon, Nucl. Instrum. Methods Phys. Res. B **246**, 269 (2006).
[45] http://www.synchrotron-soleil.fr/Recherche/LignesLumiere/LUCIA
[46] http://www.synchrotron-soleil.fr/Recherche/LignesLumiere/SEXTANTS
[47] http://www.esrf.eu/UsersAndScience/Experiments/ElectStructMagn/ID12
[48] J. J. Rehr, J. J. Kas, F. D. Vila, M. P. Prange, and K. Jorissen, Phys. Chem. Chem. Phys. **12**, 5503 (2010).
[49] J. J. Rehr and R. C. Albers, Rev. Mod. Phys. **72**, 621 (2000).
[50] J. J. Rehr, J. J. Kas, M. P. Prange, A. P. Sorini, Y. Takimoto, and F. D. Vila, C. R. Phys. **10**, 548 (2009).
[51] K. Jorissen, J. J. Rehr, and J. Verbeeck, Phys. Rev. B **81**, 155108 (2010).
[52] J. J. Kas, A. P. Sorini, M. P. Prange, L. W. Cambell, J. A. Soininen, and J. J. Rehr, Phys. Rev. B **76**, 195116 (2007).
[53] A. L. Ankudinov, Y. Takimoto, and J. J. Rehr, Phys. Rev. B **71**, 165110 (2005).
[54] K. Jorissen and J. J. Rehr, Phys. Rev. B **81**, 245124 (2010).
[55] M. P. Prange, J. J. Rehr, G. Rivas, J. J. Kas, and J. W. Lawson, Phys. Rev. B **80**, 155110 (2009).
[56] P. Blaha, K. Schwarz, G. K. H. Madsen, D. Kvaniscka, and J. Luitz, *WIEN2k, An Augmented Plane Wave + Local Orbitals Program for Calculating Crystal Properties* (Technische Universität WIEN, Austria, 2001).
[57] G. K. H. Madsen, P. Blaha, K. Schwarz, E. Sjöstedt, and L. Nordström, Phys. Rev. B **64**, 195134 (2001).
[58] E. Sjöstedt, L. Nordström, and D. J. Singh, Solid State Commun. **114**, 15 (2000).
[59] J. P. Perdew, K. Burke, and M. Ernzerhof, Phys. Rev. Lett. **77**, 3865 (1996).
[60] G. Hug, M. Jaouen, and M. W. Barsoum, Phys. Rev. B **71**, 024105 (2005).
[61] M. Ramzan, S. Lebègue, and R. Ahuja, Solid State Commun. **152**, 1147 (2012).
[62] Y. Mo, P. Rulis, and W. Y. Ching, Phys. Rev. B **86**, 165122 (2012).
[63] M. Jaouen, M. Bugnet, N. Jaouen, P. Ohresser, V. Mauchamp, T. Cabioc'h, and A. Rogalev, J. Phys: Condens. Matter **26**, 176002 (2014).
[64] M. Ramzan, S. Lebègue, and R. Ahuja, Phys. Status Solidi RRL **5**, 122 (2011).
[65] M. Dahlqvist, B. Alling, and J. Rosén, J. Appl. Phys. **113**, 216103 (2013).
[66] Y. L. Du, Z. M. Sun, H. Hashimoto, and M. W. Barsoum, J. Appl. Phys. **109**, 063707 (2011).
[67] G. Kresse and J. Furthmuller, Comput. Mater. Sci. **6**, 15 (1996).
[68] A. Togo, F. Oba, and I. Tanaka, Phys. Rev. B **78**, 134106 (2008).
[69] A. L. Ankudinov, S. I. Zabinsky, and J. J. Rehr, Comput. Phys. Commun. **98**, 359 (1996).
[70] J. C. Le Bossé, T. Epicier, and B. Jouffrey, Ultramicroscopy **106**, 449 (2006).
[71] A. L. Ankudinov, A. I. Nesvizhskii, and J. J. Rehr, Phys. Rev. B **67**, 115120 (2003).
[72] J. J. Rehr, Rad. Phys. Chem. **75**, 1547 (2006).
[73] R. D. Leapman and L. A. Grunes, Phys. Rev. Lett. **45**, 397 (1980).
[74] B. T. Thole, P. Carra, F. Sette, and G. van der Laan, Phys. Rev. Lett. **68**, 1943 (1992).
[75] F. de Groot, Coord. Chem. Rev. **249**, 31 (2005).
[76] E. Stavitski and F. de Groot, Micron **41**, 687 (2010).
[77] M. Mattesini and M. Magnuson, J. Phys: Condens. Matter **25**, 035601 (2013).
[78] T. Cabioc'h, P. Eklund, V. Mauchamp, M. Jaouen, and M. W. Barsoum, J. Eur. Cer. Soc. **33**, 897 (2013).
[79] A. Togo, L. Chaput, I. Tanaka, and G. Hug, Phys. Rev. B **81**, 174301 (2010).
[80] J. D. Hettinger, S. E. Lofland, P. Finkel, T. Meehan, J. Palma, K. Harrell, S. Gupta, A. Ganguly, T. El-Raghy, and M. W. Barsoum, Phys. Rev. B **72**, 115120 (2005).